

# Theory and simulations of rigid polyelectrolytes

Markus Deserno<sup>1a</sup>, Christian Holm<sup>2b</sup>

<sup>a</sup>*Department of Chemistry and Biochemistry, UCLA, USA*

<sup>b</sup>*Max-Planck-Institut für Polymerforschung, Ackermannweg 10,  
55128 Mainz, Germany*

## Abstract

We present theoretical and numerical studies on stiff, linear polyelectrolytes within the framework of the cell model. We first review analytical results obtained on a mean-field Poisson-Boltzmann level, and then use molecular dynamics simulations to show, under which circumstances these fail quantitatively and qualitatively. For the hexagonally packed nematic phase of the polyelectrolytes we compute the osmotic coefficient as a function of density. In the presence of multivalent counterions it can become negative, leading to effective attractions. We show that this results from a reduced contribution of the virial part to the pressure. We compute the osmotic coefficient and ionic distribution functions from Poisson-Boltzmann theory with and without a recently proposed correlation correction, and also simulation results for the case of poly(para-phenylene) and compare it to recently obtained experimental data on this stiff polyelectrolyte. We also investigate ion-ion correlations in the strong coupling regime, and compare them to predictions of the recently advocated Wigner crystal theories.

---

<sup>1</sup>email: markus@chem.ucla.edu

<sup>2</sup>email: holm@mpip-mainz.mpg.de

# 1 Introduction

“Polyelectrolytes are polymers bearing ionizable groups, which, in polar solvents, can dissociate into charged polymer chains (macroions) and small counterions” [1]. The combination of macromolecular properties and long-range electrostatic interactions produces an impressive variety of phenomena [2, 3, 4]. It makes these systems interesting from a fundamental as well as a technological point of view.

A thorough understanding of polyelectrolytes has become increasingly important in biochemistry and molecular biology. This is due to the fact that virtually all proteins, as well as the DNA, are polyelectrolytes. Their interactions with each other and with the charged cell-membrane are still far from being understood. For instance, a puzzling question is why two equally charged objects should attract each other in the first place [5].

In this article we focus on stiff linear polyelectrolytes, which we subsequently approximate by charged cylinders. This is a relevant special case, applying to quite a few important polyelectrolytes, like DNA, actin filaments or microtubules. We treat the solvent in dielectric approximation and explicitly describe only the small ions. Within Poisson-Boltzmann (PB) theory [6] and on the level of a cell model the cylindrical geometry can be treated exactly in the salt-free case [7, 8, 9, 10, 11, 12], providing for instance new insights into the phenomenon of the Manning condensation [13, 14].

The paper is organized as follows: First we review some essential features of the PB mean-field solution of the cell model. Then we discuss the applicability of PB theory to the ion distribution functions and show under which circumstances PB theory fails quantitatively (underestimated condensation) and qualitatively (overcharging, charge oscillations and attractive interactions). Next we present measurements of the osmotic pressure for the nematic phase of hexagonally packed polyelectrolytes as a function of density and compare it to PB predictions and the Manning limiting law. In the next section we study the particular case of poly(para-phenylene) by means of PB theory, including a correlation correction of the basis of a recently proposed Debye-Hückel-Hole-cavity theory (DHHC) [15], and simulational results. The results are compared to recent experimental data on this system [16, 17, 18]. We find that correlation effects enhance condensation and lower the osmotic pressure, yet are not fully able to explain the discrepancy to the experimental data. At the end we try to shed light onto the role of specific ionic correlations. Two-dimensional correlations on the surface of the rods are found to be present, but weakly developed. No hexatic order of the ions is observed.

## 2 Simulation method and model system

### 2.1 The Langevin thermostat

We utilize molecular dynamics (MD) simulations using a Langevin thermostat [19] to study the equilibrium properties of our model system within the canonical ensemble. Technically this is achieved by integrating the stochastic differential equation

$$m_i \ddot{\mathbf{r}}_i = -\nabla U(\{\mathbf{r}_i\}) - \Gamma \dot{\mathbf{r}}_i + \boldsymbol{\xi}_i(t) \quad (1)$$

on the computer, where  $m_i$  are the masses of particles with coordinates  $\mathbf{r}_i$  subject to a potential energy function  $U$ , a friction  $\Gamma$  linear in the velocity and a stochastic white noise  $\boldsymbol{\xi}_i(t)$ . The latter two can be thought of as imitating the presence of a surrounding viscous medium responsible for a drag force and random collisions, respectively. Since both effects have the same origin, they are related to each other by a simple version of the fluctuation-dissipation-theorem. This can be exploited to choose their strength such as to converge towards the canonical state:

$$\langle \boldsymbol{\xi}_i(t) \rangle = 0 \quad \text{and} \quad \langle \boldsymbol{\xi}_i(t) \cdot \boldsymbol{\xi}_j(t') \rangle = 6 k_B T \Gamma \delta_{ij} \delta(t - t'), \quad (2)$$

where  $k_B T$  is the thermal energy.

We use a standard Verlet integrator[20] to integrate (1). Time step  $\delta t$  and friction coefficient  $\Gamma$  were set to 0.01 and 1.0 in Lennard-Jones units (see below).

## 2.2 Interaction potentials

We use the purely repulsive Lennard-Jones (LJ) potential to give the counterions an excluded volume:

$$V_{\text{LJ}}(r) = \begin{cases} 4\epsilon \left[ \left( \frac{\sigma}{r} \right)^{12} - \left( \frac{\sigma}{r} \right)^6 + \frac{1}{4} \right] & : 0 < r \leq r_{\text{cut}} \equiv 2^{1/6} \sigma \\ 0 & : r_{\text{cut}} < r. \end{cases} \quad (3)$$

The advantage of including the  $-r^{-6}$  contribution instead of merely using the purely repulsive  $r^{-12}$  is that Eqn. (3) is exactly zero beyond  $r_{\text{cut}}$  and merges smoothly to this value at  $r_{\text{cut}}$ , allowing a larger time step.

The Coulomb potential of a charge  $Q$  is written as

$$\beta e_0 V_C(r) = (Q/e_0) \frac{\ell_B}{r}, \quad (4)$$

where  $\ell_B = \beta e_0^2 / 4\pi\epsilon$  is the Bjerrum length, the distance at which two unit charges have an interaction energy equal to  $1/\beta := k_B T$ ,  $e_0$  is the positive elementary charge, and  $\epsilon$  is the product of the dielectric constants of vacuum,  $\epsilon_0$ , and the medium,  $\epsilon_r$ , respectively. The Lennard-Jones unit  $\sigma$  is always used as unit of length and  $\epsilon$  is always set to the thermal energy  $k_B T$ . Temperature is implemented via the Bjerrum length. Mass is irrelevant and set equal to one – it would only be needed to translate the Lennard-Jones time  $\tau_{\text{LJ}} = \sigma \sqrt{m/\epsilon}$  into “real” time. We intend to model an aqueous environment at room temperature, which implies  $\ell_B \approx 7.14 \text{ \AA}$ .

Within the periodic boundary conditions employed during the simulations, the presence of such long-range interactions poses both mathematical and technical difficulties. We use the most efficient FFT accelerated Ewald sum, the P<sup>3</sup>M code, which scales almost linearly with the number of charges [21, 22].

## 2.3 Generating a cell-geometry

Compared to the spherical cell model, the cylindrical one presents one additional but crucial complication: the charged rod is infinitely long. Several methods have been proposed in the literature to handle this problem [23, 24, 25, 26]. They essentially all use as a unit cell a hexagonal prism with a certain height. This

approximates the cylindrical cell by a space-filling object. In the present work we take a cube of side length  $L_b$  and place a rod along the main diagonal. Upon periodically replicating this system the diagonal rod becomes infinitely long and an infinite triangular array of such replicated rods emerges. The resulting Wigner-Seitz cell of this lattice is a regular hexagon, which can alternatively be viewed as the unit cell. This is illustrated in Fig. 2. Observe that the symmetry of the replicated system is still cubic. The radius  $R$  of a circle with the same area  $A$  is then given by  $R = L_b/\sqrt{\pi\sqrt{3}}$ . This value is most appropriately used for comparing results between the hexagonal and the cylindrical cell model.

If the line charge density of the rod is  $\lambda$ , electroneutrality requires the number of  $v$ -valent counterions to be  $N = \sqrt{3}L_b\lambda/ve_0$ . Hence the average counterion density is given by  $n = N/L^3 = \sqrt{3}\lambda/ve_0L^2$  and is thus inversely proportional to  $L^2$  instead of  $L^3$ . The number of counterions can therefore be written as  $N = (\sqrt{3}\lambda/ve_0)^{3/2}n^{-1/2}$ , which implies that a smaller density requires more particles. While this makes the simulation of dilute systems rather expensive, it gives at the same time rather small dense systems. The latter problem can be circumvented by combining blocks of  $2 \times 2 \times 2$ ,  $3 \times 3 \times 3$  or even more elementary cubes to a big cube and using the latter as the unit box for the periodic boundary conditions.

The ratio between  $\ell_D = (4\pi\ell_B v^2 n)^{-1/2}$  (the average Debye length of the counterions) and the rod separation  $d_{\text{rod}}$  can be written as

$$\frac{\ell_D}{d_{\text{rod}}} = (8\pi\xi v/\sqrt{3})^{-1/2} \approx 0.2625/\sqrt{\xi v}, \quad (5)$$

where the definition of the Manning parameter  $\xi := \lambda\ell_B/e_0$  was used, see also Sec. 3. Obviously, for strongly charged rods the Debye length is smaller than the separation of the two rods. Even for  $\xi v = 1$  it is only half as large as the distance between rod axis and Wigner-Seitz boundary, and the neighboring cells effectively decouple. This statement is independent of density.

## 3 Poisson-Boltzmann Essentials

### 3.1 The Poisson-Boltzmann Solution

At this stage we want to briefly recall the necessary knowledge about the PB solution of the cylindrical cell model [7, 9, 10, 11, 12]. Consider an infinitely long cylinder of radius  $r_0$  and line charge density  $\lambda > 0$ , coaxially enclosed in a cylindrical cell of radius  $R$ . Global charge neutrality of the system is ensured by adding an appropriate amount of oppositely charged  $v$ -valent counterions. In the following only the case of no extra salt will be discussed.

Within PB theory the individual counterions are replaced by a cylindrical counterion density  $n(r)$ , where  $r$  denotes the radial distance from the cylinder axis. Defining the reduced electrostatic potential  $y$  and the screening constant  $\kappa > 0$  as

$$y(r) = \beta e_0 v \psi(r) \quad \text{and} \quad \kappa^2 = 4\pi\ell_B v^2 n(R), \quad (6)$$

the PB equation can be written as

$$y'' + \frac{y'}{r} = \kappa^2 \exp(y). \quad (7)$$

It will be useful to define the dimensionless *Manning parameter*  $\xi = \lambda \ell_{\text{B}}/e_0$  which counts the number of unit charges on the rod per Bjerrum length. In the following the main focus will be on the strongly charged case characterized by  $\xi v > 1$ . Fixing the two boundary conditions for the electric field,

$$y'(r_0) = -2\xi v/r_0 \quad \text{and} \quad y'(R) = 0, \quad (8)$$

the correctly normalized solution to Eqns. (7,8) can be written as [7, 11, 12]

$$y(r) = -2 \ln \left\{ \frac{r}{R} \sqrt{1 + \gamma^{-2}} \cos \left( \gamma \ln \frac{r}{R_{\text{M}}} \right) \right\}. \quad (9)$$

Insertion of the general solution from Eqn. (9) into the boundary conditions from Eqn. (8) yields two coupled transcendental equations for the two integration constants  $\gamma$  and  $R_{\text{M}}$ :

$$\gamma \ln \frac{r_0}{R_{\text{M}}} = \arctan \frac{1 - \xi v}{\gamma} \quad \text{and} \quad \gamma \ln \frac{R}{R_{\text{M}}} = \arctan \frac{1}{\gamma}. \quad (10)$$

Subtracting the left part from the right part in Eqn. (10) eliminates  $R_{\text{M}}$  and provides a single equation

$$\gamma \ln \frac{R}{r_0} = \arctan \frac{1}{\gamma} + \arctan \frac{\xi v - 1}{\gamma}, \quad (11)$$

from which  $\gamma$  can be obtained numerically. The second integration constant  $R_{\text{M}}$ , which will be referred to as the Manning radius, can be obtained from either one of the Eqns. in (10) as soon as  $\gamma$  is known. Note finally that  $\kappa$  and  $\gamma$  are connected via

$$\kappa^2 R^2 = 2(1 + \gamma^2). \quad (12)$$

Since the  $\xi$  and  $v$  only enter in the combination  $\xi v$ , changing valence or electrostatic interaction strength is equivalent on Poisson-Boltzmann level. In particular, at given cell geometry  $\{r_0, R\}$  the Manning radius  $R_{\text{M}}$  is a unique function of  $\xi v$ . Eqn. (11) implies the sequence of inequalities  $\ln(R/r_0) \leq \pi/\gamma \leq \ln(R/r_0) + \xi v/(\xi v - 1)$ . The resulting asymptotic for  $\gamma$  in the dilute limit  $R \rightarrow \infty$  gives rise to what is often called the ‘‘Manning limiting laws’’.

The integrated probability distribution of finding a mobile ion at distance  $r$  within a cylinder of radius  $r \in [r_0, R]$  can be determined analytically by integrating the charge density:

$$P(r) = \frac{1}{\lambda} \int_{r_0}^r dr' 2\pi r' e_0 v n(r') = \left(1 - \frac{1}{\xi v}\right) + \frac{\gamma}{\xi v} \tan \left( \gamma \ln \frac{r}{R_{\text{M}}} \right). \quad (13)$$

This is the fraction of counterions found within a cylinder of radius  $r$ .  $P(r)$  will be referred to as counterion distribution function. At  $r = R_{\text{M}}$  the last term in  $P$  vanishes, giving the Manning fraction  $f_{\text{M}} := 1 - 1/\xi v$  of ions within  $R_{\text{M}}$ . These are the ions which can not be diluted away, if the cylinder radius is sent to infinity. This phenomenon is referred to as *Manning condensation* [13, 14].

### 3.2 How to quantify counterion condensation

If the counterion distribution function  $P$  is known, the condensed counterion fraction can be characterized in the following “geometric” way: Eq. (13) shows that  $P$  viewed as a function of  $\ln(r)$  is merely a shifted tangent-function with its center of symmetry at  $(\ln(R_M); f_M)$ . Since, however,  $\tan''(0) = 0$ , Manning radius and Manning fraction can be found by plotting  $P$  as a function of  $\ln(r)$  and localizing the point of inflection.

This property of  $P$ , derived within the framework of PB theory, can in turn be used to *define* the condensed fraction [27, 12]. It provides a suitable way to quantify counterion condensation beyond the scope of PB theory, and it is exact in the salt-free PB limit. From here on this method will be referred to as the *inflection point criterion*. It has the advantages of (i) not fixing by definition the amount of condensed counterions ( $f_M$  and  $R_M$  can be determined independently of each other), (ii) reproducing the salt-free PB limit, and (iii) quantifying the breakdown of the coexistence of condensed and uncondensed counterions in the high salt limit.

## 4 Generic ion distribution functions

On the plain PB level the radius  $r_0$  of the rod is not a completely independent variable, since it enters only in the combination  $R/r_0$ , see Eqn. (11). The rod in our simulation is built up from a sequence of small Lennard-Jones particles lined up along the main diagonal of the simulation cell. The distance of closest approach of two Lennard-Jones particles can then be identified with the radius  $r_0$  of the rod and yields an effective rod radius of  $\sigma$ .

Upon leaving the PB level, the ratio between counterion diameter  $\sigma$  and rod radius  $r_0$  becomes relevant, which has for instance been investigated in Ref. [25, 28]. Here we do not intend to perform a systematic investigation of such effects, but instead present later in Sec. 6 results for systems mapped to physically relevant parameters, DNA and two kinds of poly(p-phenylenes), in which the rod has a considerably larger diameter than the counterions.

### 4.1 Density dependence within monovalent systems

At fixed rod radius of  $r_0$  the relevant variable  $R/r_0$  is changed by varying the cell size  $R$  and therefore the density. Here we present results for such a density scan for systems with  $\ell_B/\sigma \in \{2, 3\}$ . The monovalent and positively charged particles forming the rod were placed along the main diagonal with a center-center distance of  $1.04245\sigma$ , giving a line charge density of  $\lambda = 0.959279 e_0/\sigma$ . In connection with the two presented values for the Bjerrum length this yields Manning parameters of  $\xi = 1.919, 2.878$  and corresponding Manning fractions of  $f_M = 1 - 1/\xi = 0.4788, 0.6525$  in the monovalent case. The cell radius  $R$  has been varied between  $2.06\sigma$  and  $124\sigma$ , which for monovalent counterions corresponds to average ion densities of  $7.2 \times 10^{-2}\sigma^{-3}$  and  $2.0 \times 10^{-5}\sigma^{-3}$ , respectively. The inflection point criterion from Sec. 3.2 has been used to determine the radial extension of the condensed layer,  $R_M^*$ , and the fraction of ions within it,  $f_M^* = P(R_M^*)$ , where the star denotes the measured quantities. A graphical illustration of the distribution functions is given in Fig. 3.

The important things to observe are the following. The measured condensed fraction  $f_M^*$  is always larger than the fraction predicted by the PB theory. However, the fraction from the simulation decreases monotonically with decreasing density towards the Manning limit  $f_M$ . Such a deviation is to be expected, since PB is essentially a low density theory [29, 30].

In contrast to the clear tendency of the measured condensed fraction to decrease upon dilution, the behavior of the condensation radius  $R_M^*$  appears to be more complicated. There does not seem to exist a simple monotonic convergence of  $R_M^*$  towards  $R_M$ . Rather, for high densities the measured condensation distance is larger than the Manning radius, while for the investigated low densities it is smaller. Unfortunately, a clear-cut statement is difficult since the localization of the point of inflection in  $P$  as a function of  $\ln(r)$  is only possible with an error estimated to be of the order of 1%.

For Bjerrum length  $\ell_B = 1\sigma$ , corresponding to  $\xi = 0.9593 < 1$ , the radial distribution functions are compared to the PB predictions in Fig. 4. It can be seen that the measured and PB predicted distributions almost coincide for all cell sizes under investigation. While this is to be expected for low densities, the remarkable agreement at high densities is somewhat surprising. Apparently, PB theory is a fairly good description of weakly charged systems, i.e., ones which are below the Manning threshold.

## 4.2 Fitting to a generalized Poisson-Boltzmann distribution

Since the measured Manning radius  $R_M^*$  can be smaller than the PB prediction, but  $f_M^* > f_M$  and  $R_M^* < R_M$  is incompatible with PB theory, it is impossible to describe such a measured  $P(r)$  with a PB distribution function in which a somewhat enlarged effective Manning parameter  $\xi^*$  is used. Nevertheless, it would be desirable to use at least some of the knowledge about the ion distribution function from PB theory for evaluating relevant observables in a simulation or in a real experiment. To the lowest order, e.g., within a two state model, the increase of counterion condensation can be ascribed to such an effective  $\xi^*v = 1/(1 - f_M^*)$ . To break the monotonic connection between  $f_M$  and  $R_M$  one assumes that the functional form of  $P$  is given by the PB form in Eqn. (13), but neglects the relation in Eqn. (11). Using Eqn. (10i), this suggests fitting the measured distribution in a region around the inflection point to the form

$$P_{\text{fit}}(r) = 1 - \frac{1}{\xi^*v} + \frac{\gamma^*}{\xi^*v} \tan \left( \gamma^* \ln \frac{r}{r_0^*} + \arctan \frac{1 - \xi^*v}{\gamma^*} \right) \quad (14)$$

with the three fit parameters  $\xi^*$ ,  $\gamma^*$  and  $r_0^*$ .<sup>3</sup> The condensed fraction is then given by  $f_M^* = 1 - 1/\xi^*v$  and the condensed radius by  $R_M^* = r_0^* \exp\{\arctan[(\xi^*v - 1)/\gamma^*]/\gamma^*\}$ . Fig. 5 illustrates this procedure for one system. While this approach might seem to be very powerful, it suffers from the drawback that the actual numbers depend on the chosen fitting region. Nevertheless, it provides an independent way of quantifying condensation and can even be applied to very noisy

<sup>3</sup>It might seem strange to regard the rod radius as a free parameter, but there are two reasons for this. First, this does not force the fit to coincide with the PB form outside the chosen fitting-region. Second, not even in a real experiment is the radius of a macroion always known in advance. Rather, it is often necessary to obtain this information within the same measurement [16].

data, for which the localization of an inflection point in  $P$  as a function of  $\ln(r)$  is otherwise virtually impossible.

### 4.3 Multivalent ions

The universal dependence of the ion distribution on the product  $\xi v$  is an artifact of Poisson Boltzmann theory. Fig. 6 shows examples of systems with different Manning parameters but the same value of  $\xi v$ . Not only is the condensation enhanced as compared to PB theory, but the enhancement is stronger for the case involving multivalent ions. For instance, in the dense trivalent system the condensation is enhanced by 30% with respect to the PB prediction.

The reason is that at given charge density multivalent systems have a lower number density and thus fewer particles. This lowers any kind of excluded volume interactions, and also makes the entropic contribution less pronounced. Moreover, the relevant variable for describing the strength of correlation effects is  $\ell_B v^2$  [15]. Hence, an increase in valence is more important than an increase in Bjerrum length.

Within PB theory the expression for the contact density  $n(r_0)$  in the limit of infinite dilution is given by

$$n(r_0) \stackrel{R \rightarrow \infty}{=} 2\pi\ell_B\tilde{\zeta}^2 \left(1 - \frac{1}{\xi v}\right)^2, \quad (15)$$

where  $e_0\tilde{\zeta}$  is the surface charge density of the rod. For high rod charge this expression becomes independent of valence. Hence, replacing monovalent counterions by multivalent ones reduces their total *number* in the cell, but for a highly charged rod not their *density* at the rod surface. This result is a consequence of the contact value theorem and thus holds beyond the Poisson-Boltzmann approximation[9].

### 4.4 Addition of salt

The influence of salt on the distribution functions has been discussed within the PB theory in detail in Ref. [12]. The general finding was that a low salt content leaves the picture of Manning condensation qualitatively unchanged, while at increasing salt concentration a crossover between Manning condensation and simple salt-screening occurs.

If one starts adding  $N$  salt molecules to the salt free solution one finds that the inflection point gets shifted to smaller values of  $r$ , hence the layer of condensed counterions contracts. The second finding is that the *amount* of condensation is only marginally increased. From a certain  $N$  on two more inflection points appear close to the cell boundary. This happens typically for a corresponding Debye length being of the order of the cell size itself, indicating the appearance of a characteristic, salt induced, change in the convexity of  $P$  (as a function of  $\ln r$ ). Upon a further increase in  $N$  one of the two new inflection points shifts towards smaller values of  $r$ , finally fusing with the Manning inflection point and “annihilating” it. Roughly speaking, the inflection points vanish if the Debye length characterizing the salt content becomes smaller than the radius of the condensed layer. In this case it is no longer meaningful to distinguish between condensed and uncondensed counterions. Indeed, for a very high salt



content, where the Debye length is much smaller than the radius of the rod, the solution of the PB equation would be the one of a charged plane and one may consider all excess counterions being condensed – no matter what the charge density of the rod is.

For three systems with numbers of salt molecules  $N \in \{0, 104, 3070\}$  a simulation has been performed and compared to the PB prediction in Fig. 7. As in the salt-free case the computer simulations show a more pronounced condensation effect towards the rod. Nevertheless, the shape of the distribution functions remains qualitatively the same. Note in particular that the appearance and disappearance of two points of inflection at  $N = 104$  and  $N = 3070$  respectively, which leads to extremely small curvatures in the PB distribution functions, also leads to very straight regions in the measured distribution functions. The crossover from Manning condensation to screening, as described within the PB theory, can be expected to be essentially correct. It should not be overlooked, however, that the addition of salt ions will affect the distribution function much more dramatically if their valence is larger than the valence of the counterions. In this case, the salt counterions will accumulate in the vicinity of the rod at the expense of the lower valent “real” counterions as has previously been demonstrated in a system with a valence mixture of counterions [31].

The PB approach fails to describe the physical situation if one or more of the following conditions apply: (i) the electrostatic interactions are strong, (ii) the counterions are multivalent or (iii) the density is high. Results of a simulation under such conditions can be seen in Figure 8. Here, a system with box length  $L_b/\sigma = 36.112$ , i.e., 60 monovalent counterions and a cell size of  $R/\sigma = 15.481$ , and  $\ell_B/\sigma = 4.1698$ , i.e.,  $\xi = 4$ , has been investigated after adding 1000 molecules of a 2:2 salt. Since this gives almost 17 times as much salt as counterions and a salt Debye length of  $\ell_D/\sigma = 0.33 \ll R/\sigma$ , this can essentially be viewed as a charged rod in a bulk 2:2 electrolyte. The most characteristic feature of the charge distribution function is that it overshoots unity, showing a charge reversal of the rod at distances around  $r \approx 1.5\sigma$ , while the simple PB prediction is clearly qualitatively off. This phenomenon is usually referred to as overcharging and has been predicted for the rod geometry first from hypernetted chain calculations [32] and later by a modified PB approach [33, 34], and has also been observed in planar geometries [35]. Since  $P(R) = 1$  for the reason of global electroneutrality, the overshooting above 1 at small distances implies the existence of a range of  $r$ -values at which the mobile ion system is locally positively charged, i.e., with the same charge as the rod, such that  $P(r)$  can eventually decay to 1. This is seen in the right frame of Fig. 8, which shows that  $n_{+2}(r) > n_{-2}(r)$  at  $r \approx 2\sigma$ . Since  $P(1.5\sigma) \approx 1.45$ , the rod and its innermost layer of condensed ions could be viewed as an effective rod of radius  $1.5\sigma$  which is negatively charged with Manning parameter  $\xi = 1.8$ . Since this value is again larger than 1, it entails ion condensation, but this time of positive ions. In fact, it even leads to a second overcharging, as can clearly be seen in Fig. 8, where  $P(r)$  – in decaying from 1.45 – overshoots the value of 1 again. Overcharging can thus give rise to layering. In the presented example no less than three layers can clearly be made out. These local charge oscillations also reflect themselves in oscillations of the electrostatic potential, as demonstrated in the inset in the right frame of Fig. 8. Notice that these oscillating potentials will also have pronounced effects on the interaction between such rigid polyelectrolytes. HNC/MSA theory can qualitatively and quantitatively describe such effects to a very good degree, as

has been demonstrated theoretically a long time ago [32]. A recent comparison with simulations can be found in Ref. [36].

## 5 Pressure

### 5.1 Pressure measurements within the generic model

Using the results from the Appendix A we now turn towards pressure measurements for the generic systems described above. Because of the periodic boundary conditions, we are actually looking at the pressure of a nematic, hexagonally packed solution of charged rods. We specifically compute the dimensionless osmotic coefficient  $\hat{p}$ , which is simply the pressure normalized by its ideal gas contribution

$$\hat{p} = \frac{p}{p^{\text{ig}}} = \frac{p}{nk_{\text{B}}T}. \quad (16)$$

For an *isolated* cell the pressure is given by the particle density at the outer cell boundary. This is a rigorous statement, true for the spherical, cylindrical and planar cell model [9]. It is a merit of the PB equation that it retains the validity of this exact relation. For the extended density functional theories this no longer holds and additional terms appear [29].

Within Poisson-Boltzmann theory the osmotic coefficient as determined from the boundary density is

$$\hat{p} = \frac{1 + \gamma^2}{2\xi v} \stackrel{R \rightarrow \infty}{\rightrightarrows} \frac{1}{2\xi v}, \quad (17)$$

where  $\gamma$  is the density dependent integration constant from Eqn. (11),

Fig. 9 illustrates these measurements for monovalent counterions and three values of  $\ell_{\text{B}}/\sigma = 1, 2, 3$ . Several things may be noted: The osmotic coefficient from the simulations is always smaller than the PB prediction, but for low density both values converge. This also illustrates that the Manning limiting law from the r.h.s of Eqn. (17) becomes asymptotically correct for dilute systems. Upon increasing the density, the osmotic coefficient rises weaker than the PB prediction. This is more pronounced for systems with higher Bjerrum length, and consequently, higher Manning parameter, and is due to enhanced counterion condensation which has been observed in Sec 4. Notice that this has a very remarkable side-effect. Over a considerable range of densities the measured osmotic coefficient is much closer to the limiting law than to the actual PB prediction. This makes the Manning limit look much more accurate than it really ought to be. However, the surprising effect should not be over-interpreted, since the underlying reason is nothing but a fortunate cancellation of two contributions of approximately the same size which are not contained in the limiting laws.

Also for the pressure it is interesting to investigate complementary systems in which the values of Bjerrum length  $\ell_{\text{B}}/\sigma$  and valence  $v$  have been interchanged to keep the product  $\xi v$  fixed. However, at given density the cell radius depends on the valence, so  $\hat{p}(n)$  does no longer universally depend on this product. Since in the limit of high density  $\hat{p}$  is easily seen to increase with density, while at low density it decreases, the functions  $\hat{p}(n)$  for different valences intersect at some point.

Fig. 10 summarizes the results of measurements on the multivalent systems with  $v = 1, 2, 3$ , which yield the same values of  $\xi v$  as the monovalent ones investigated before. The most striking feature is the appearance of a negative osmotic coefficient in a certain density region of the trivalent case. If the constraint of a fixed rod-separation were to be replaced, the system would phase separate, hence, attractive interactions must be present between the rods. Similar observations have been reported in Refs. [24, 25, 26]. In order to trace back the origin of those attractions, Fig. 11 displays the osmotic coefficient in the divalent and trivalent cases, split into two contributions: *(i)* the non-electrostatic part comprising ideal gas contribution and the short-range virial and *(ii)* the electrostatic part, which for visual convenience is plotted with a reversed sign. Hence, the difference between those two curves gives the curves in Fig. 10. We observe that the electrostatic part leads to a monotonically increasing attraction with increasing density. It is almost twice as strong in the trivalent case. The very strong increase of the osmotic coefficient at large densities is due to the virial, i.e., due to repulsive ion-rod and ion-ion interactions. The measured negative pressure in the trivalent case is the result of a “sudden” drop in the virial contribution. Nothing particular can be observed in the electrostatic part. We suggest the explanation that in an intermediate range of densities the presence of surrounding rods lifts condensed ions from the surface they are pushing on, thereby reducing the short range excluded volume contribution. In too dilute systems this effect is not operative, while in too dense systems the effect of the other rods is actually to push ions more closely to the surface. Hence, there is a density range in which the virial is reduced by the presence of other rods.

Contrary to the simulations, the osmotic coefficient from the PB theory is always positive. This is the consequence of the rigorous proof that such attractive interactions are absent on the PB level [37]. An extension of this statement to ions of finite size and to a wider class of boundary conditions and density functionals can be found in Ref. [38].

Finally it should be noted that the above measurements can not be used to infer that attractive forces between charged rods require the counterions to be at least trivalent. The reason is twofold: First, at given valence one can vary Bjerrum length and line charge density. Increasing the Manning parameter will lead to negative pressure in the divalent system. Second, keeping all interaction potentials fixed, the radius  $r_0$  of the charged rod is a relevant observable, as has been demonstrated in Ref. [25]. Hence, a general statement about presence or absence of attractive interactions is difficult, since a five-dimensional parameter space is involved:  $\{\lambda, \ell_B, v, r_0, n\}$ .

## 6 Examples: poly(p-phenylene)

This section discusses simulations in which the parameters are explicitly mapped to an experimental system. This affects the values of ion diameter  $\sigma$ , rod radius  $r_0$ , Bjerrum length  $\ell_B$  and line charge density  $\lambda$ . In order to have  $r_0$  different from  $\sigma$ , we use as the ion-rod-potential a LJ like expression, in which  $r$  is replaced by  $r - r_s$  and the shift  $r_s$  is related to the desired rod radius by  $r_0 = r_s + \sigma/2$ .

Since these systems have been investigated either in the presence of salt or at rather high Manning parameter, the phenomena happening in the vicinity of the rod are always well decoupled from the cell boundary. Therefore, an even

simpler geometry has been chosen: One rod placed parallel to one of the edges of a cubic simulation cell.

### 6.1 Distribution functions and osmotic coefficient for salt free poly(p-phenylene) solutions

The Manning limiting laws are claimed to apply in the limit of low density. However, an experimental verification of this effect using DNA as rod-like polyelectrolytes is difficult, since the double helix starts to unwind at low ionic strength. It would therefore be desirable to have a stiff model polyelectrolyte which does not suffer from this problem. One such system belonging to the class of poly(para-phenylenes) (ppp) has recently been investigated in Refs. [16, 17]. The constitution formula is given in Fig. 1. The fully aromatic backbone exhibits an excellent chemical stability and has a persistence length of approximately 20 nm. The degree of polymerization used in the abovementioned studies was between 20 and 40, so that the contour length equals approximately one persistence length at most. The dominant contribution to the signal in small angle X-ray scattering experiments stems from the iodine ions, since the excess electron density of the backbone is very low. Table 1 lists four systems which have been simulated based on a mapping to ppp.

In a first step the simulated ion distribution functions shall be compared with the PB prediction as well as with the Debye-Hückel-hole-cavity theory from Ref. [15], which tries to incorporate correlations missing in the PB approach. Figure 12 shows the corresponding distribution functions for the systems from Table 1. Qualitatively the PB prediction is already a good description of those systems, if one graciously disregards the inevitable problems at the cell boundary. However, the presence of correlations shifts the distribution functions up in all four cases. Since this shift is rather small, i.e., the correlations are weak, the Debye-Hückel-hole-cavity theory is in fact an excellent description of those systems. Observe, for instance, that in the weakly charged dilute case its prediction can no longer be distinguished from the simulated curve on the chosen scale.

With the help of the condensation criterion from Sec. 3.2 the extent of the correlation-enhanced condensation can be further quantified. The Manning fraction from the molecular dynamics simulation increases only by a fairly small amount. It is at most 4% larger than the PB value. This translates to an effective Manning parameter  $\xi_{\text{eff}} = 1/(1 - f_M)$  being 5–10% larger than the bare one. This increase is very accurately captured by the Debye-Hückel-hole-cavity theory. Its prediction for  $f_M$  is at most 1% smaller than the value obtained in the simulation. Interestingly, it is even independent of density. This, however, is not a feature to be generally expected and should therefore not be over-interpreted.

In a second step the osmotic coefficients of the four model systems have been computed. Two distinct approaches have been used for analyzing the simulation results: The first computes the pressure from the stress tensor, as described in detail in Appendix A. The second approach exploits the connection from Eqn. (17) between osmotic coefficient, Manning parameter and the integration constant  $\gamma$  of the PB equation. The idea is to use the fitting procedure described in Sec. 4.2 and from that obtain values  $\xi^*$  and  $\gamma^*$ , leading to the osmotic coefficient  $(1 + \gamma^{*2})/2\xi^*$ . The most straightforward approach of measuring the boundary density is less recommendable, since in the simulation the boundary

has a quadratic and not a circular cross section, i.e., the merely approximate representation of the cell model becomes most visible and questionable here. In contrast to that, the two other approaches “look” at regions of the cell, which are away from the boundary. For comparison, also the predictions from the Manning limiting law and the full PB expression are calculated. For the two dilute systems there also exist measurements in Ref. [17] of  $\hat{p}$  via osmometry, while for the dense systems this was unfortunately impossible due to counter diffusion problems. Table 2 collects the coefficients for comparison.

The first thing which should be noted is that PB theory gives again a surprisingly good description of the measured coefficients, including the experimentally determined one. A closer look reveals that – as expected – it overestimates  $\hat{p}$ , and the deviations are larger for the dense systems. Still, PB theory is off by only 7% or 18% for the dilute or dense systems, respectively, thereby confirming the observation already made when looking at the distribution functions. A further indication of this point is that the Manning limit  $1/2\xi$  appears to be a lower boundary, which is also in accord with the pressure measurements on the generic systems with monovalent ions from Sec. 5.1. Since there it has also been found that the Manning limit need no longer act as a boundary in the multivalent case, see Fig. 10, it would be very interesting to perform experiments on those systems with, e.g., divalent ions. Observe that the experimental value of  $\hat{p}$  for the highly charged dilute system 2 is already at the Manning limit.

Since the experimentally determined osmotic coefficient appears to be smaller even than the molecular dynamics results, this indicates effects to be relevant which go beyond the model used for simulation. Most obvious candidates for this are the neglect of additional chemical interactions between the ions and the polyelectrolyte as well as solvation effects, i.e., interactions between the ions or the polyelectrolyte with the water molecules from the solution. It is for instance demonstrated in Ref. [17] that the osmotic coefficient also depends on whether one uses chlorine or iodine counterions. While one could certainly account for the different radii of these ions when computing the distance of closest approach entering the PB equation, the implications of the different hydration energies is much less obvious to incorporate and in principle requires very expensive all-atom simulations. See also the discussion in Ref. [18], which includes the effects of small excess salt to the osmotic coefficient.

Finally it should be noted that the two different methods of analyzing the molecular dynamics data lead to very similar results. While this fact is not particularly useful in a simulation, its consequences for the analysis of experimental data seem promising. In Ref. [16] poly(p-phenylene) solutions are investigated by means of small angle X-ray scattering, which due to the rod-like geometry turns out to be sensitive to the radial ion distribution function. Therefore, the measured structure factors can be related to PB distribution functions with effective values of  $\xi$ ,  $\gamma$  etc. Fitting the scattering intensity and thereby determining those values permits in principle a measurement of the osmotic coefficient along the lines already described above. What makes this approach so attractive is that it could ideally complement osmometry. If the density becomes too large, the latter suffers from severe problems with counter diffusion, but it is exactly this high density which meets the requirements of good contrast necessary for scattering.

A similar fitting procedure has been applied to the measured data from small angle X-ray scattering experiments on the systems 3 and 4; see also Ref. [16].

From a fit to the structure factor the radius  $r_0^*$  of the rod has been determined. The integration constant  $\gamma^*$  and the Manning parameter  $R_M^*$  follow from the PB theory. The obtained values are listed in Table 3. The resulting Manning radius is surprisingly close to the one determined by simulation, particularly for the system with  $\xi = 3.32$ . The osmotic coefficients constructed from the PB formula are less accurate, 10-20% too large.

## 7 The importance of correlations

We have seen that the nonlinear PB equation suffers from systematic deviations in strongly coupled or dense systems. It underestimates the extent of counterion condensation and at the same time overestimates the osmotic coefficient. The common reason for both problems is the neglect of correlations: More elaborate theories [32, 33, 15] which try to incorporate correlations reproduce the trends of the simulations, because they favor an increase in density close to the macroion surface, thereby leading to a stronger condensation and a concomitant drop in the boundary density and thus pressure.

On the one hand there is general agreement about the presence of correlations being liable for the failure of PB theory. On the other hand, this insight does not shed any light onto the question, which kind of correlations are important. In the following we investigate a simple pair-correlation function based on a one-rod property.

If the surface charge density of the rod is high, a fairly large number of counterions will stay within a condensed layer of small radial extent. Addition of salt will further increase the ionic density in this layer. It is clear that beyond a certain point (high  $\lambda$ , high  $\ell_B$  or enough salt) the ions will no longer distribute independently of each other but get locally correlated. This effect will now be measured for a DNA-like system, because for those systems correlation effects are assumed to play a prominent role. The rod radius was chosen to be  $7.86 \text{ \AA}$  ( $1.85\sigma$ ) and the ion diameter is correspondingly  $4.25 \text{ \AA}$  ( $1\sigma$ ). In addition 0.5 mol/l of a 2:2 salt has been added in excess to the divalent counterions. More information about these systems can be found in Table 4.

The first issue is to define the innermost layer. For this, a distance from the rod is chosen which contains many counterions but virtually no co-ions. A distance of roughly  $11.5 \text{ \AA}$  from the rod axis turned out to be suitable. This is about a third ion diameter farther out than the distance of closest approach. To avoid difficulties with remaining co-ions, only the counterions within this distance are taken into account in all what follows. In a second step the coordinates of those ions are radially projected onto the surface of the cylinder of closest approach, and this surface is then rolled out to a flat plane, see Fig. 13 for an illustration of this procedure. Finally, the two-dimensional pair correlation function  $g(r)$  of these projected points is computed.

One might object that the unrolled flat plane leads one to believe that the pair correlation function does only depend on distance, while in reality such a rotational symmetry cannot be expected, due to the rod curvature. However, an investigation of  $g(\mathbf{r})$  revealed that the pair correlation function is in fact rotationally symmetric up to essentially a distance which corresponds to half the circumference of the cylinder of closest approach, which is roughly  $30 \text{ \AA}$ . Larger distances can of course only be realized along the rod instead of around



it. A possible reason for this surprising symmetry is that at short distances the curvature is not yet perceptible while at large distances the particles are already uncorrelated.

Figure 14 shows the measured  $g(r)$  for four differently charged systems with Manning parameter 10.5, 8.4, 6.3, and 4.2. The last value corresponds to DNA in aqueous solution. The most important thing to observe is that for the strongly charged systems  $g(r)$  shows definite signs of correlations. Apart from the trivial correlation hole at small  $r$  there is a distance  $r_{\max}$  at which ions are more likely to be found than under the assumption of independent distribution. Notice that the maximum in  $g(r)$  is not located at  $r \approx \sigma$  but much farther out. Hence, its existence is not merely an artifact of close packing of repulsive Lennard-Jones spheres. However, if the condensed ions are assumed to form a triangular lattice on the surface in order to maximize their mutual repulsion, the resulting distance  $d_{\Delta}$  is 25 - 35 % larger than  $r_{\max}$ . Together with the only weakly pronounced oscillations in  $g(r)$  this proves the correlation induced interactions to be rather short-ranged, yet less local than a pure hard core. In any case, the range is several times larger than the average salt Debye length  $\ell_D \approx 0.5 \sigma$ .

Such two-dimensional pair correlation functions for mobile ions adsorbed on charged planes have recently been investigated theoretically in Ref. [39]. The mean separation  $d_{\zeta} = (ve_0/\zeta)^{1/2}$  of  $v$ -valent ions on the completely neutralized plane of surface charge density  $\zeta$  is identified as the important scaling length. The main predictions for the strongly coupled regime  $\Gamma_2 = \ell_B v^2/d_{\zeta} > 1$  are: (i),  $g(r)$  should have a single first peak at a distance about the size  $d_{\zeta}$  of the correlation hole. (ii), the breadth of this peak should decrease with  $\Gamma_2$  while its maximum should increase. This trend is indeed seen to be true for the functions in Fig. 14, only  $d_{\zeta}$  is roughly 10–20% larger than the actual peak position. One might want to argue that the presence of much salt entails a further increase of the layer density on top of the usual Gouy-Chapman prediction, but the results obtained in Ref. [39] are claimed to be independent of the bulk ionic strength, if the latter is smaller than the layer density. This is here the case, even though not always by an order of magnitude. An alternative explanation may be based on the presence of co-ions: Although there reside very few of them within the innermost condensed layer, there will be an appreciable amount beyond and possibly very close to  $r_1$ . Those ions can act as “bridges”, they attract counterions and thereby reduce the average closest distance between them.

Although  $r_{\max} < d_{\Delta}$ , this does not exclude a local hexatic ordering of the counterions. But since  $g(r)$  is on average rotationally symmetric, establishing signs for this requires the investigation of a suitable 3-point correlation function. The trick is to break the rotational symmetry, which suggests the following procedure:  $g(r)$  is proportional to the probability of finding a particle at a distance  $r$ , given that there is also a particle at the origin. Now define  $g_{\rightarrow}(r)$  to be proportional to the probability of finding a particle at position  $\mathbf{r}$ , given that there is also a particle at the origin *and* given that the particle which is closest to the origin is situated to the right side. This definition is further restricted to be sensitive only for next nearest neighbors and not arbitrary other particles. Thence, it answers the question: “If the nearest neighbor is on the right side, where is the next nearest neighbor?” A scatter plot of this observable is shown in the left part of Fig. 15. For this, the most highly charged DNA-sized system with Manning parameter  $\xi = 10.5$  has been used. Clearly visible are the two correlation holes around the origin and the nearest neighbor as well as a tendency

of the next nearest neighbor to be on the side opposing the nearest neighbor. All those effects are trivially explained. However, on top of that no preferential ion accumulations in the “hexatic directions” indicated as dotted lines is perceptible. The right part of Fig. 15 shows the probability distribution of finding the next nearest neighbor at an angle  $\phi$  with respect to the line joining nearest neighbor and origin. The correlation hole generated by the nearest neighbor is visible, but no increase in  $p(\phi)$  at  $60^\circ$ ,  $120^\circ$  or  $180^\circ$ . Rather, the measured data are compatible with a fairly structureless distribution, as indicated by the solid line.

Since the most strongly charged system does not show hexatic order, it will certainly be absent in the other ones. However, the coupling constant  $\Gamma_2$  introduced above has a value only about 3 in the system with Manning parameter  $\xi = 10.5$ . For larger values of  $\Gamma_2$  one would not only expect much stronger correlations and hexatic ordering but even crystallization of the adsorbed counterions into a two-dimensional Wigner crystal [39, 40]. More extensive investigations to clarify the role of correlations are presently under way [41]

## 8 Summary

Theoretical and numerical studies of stiff linear polyelectrolytes within the framework of a cell model have been presented. We outlined methods to quantify condensation for general measurements of ion distribution functions via an inflection point criterion and by using a generalized PB fit function. We compared our simulational results to predictions from mean-field PB theory, and found excellent agreement for weakly charged systems. The enhanced counterion condensation caused by ionic correlations and its dependence on parameters such as density, Bjerrum length, valence and ionic strength was measured, and effects which qualitatively go beyond mean-field theory, e.g., charge reversal and attractive interactions between like-charged macroions have been found. For systems with a high salt content, integral equation theories have proved to give a good qualitative and quantitative description of such systems [32, 36]

For the osmotic pressure measurements we displayed for a large density range that the measured pressure stays close to the Manning limiting law prediction due to a fortunate error cancellation of neglected ionic correlations and density effects which point in different directions. We showed for the specific example of a ppp-polyelectrolyte what differences to a PB description can be expected for both, the ionic distribution and the osmotic pressure. We finally analyzed some correlations for a DNA-like system, and showed that they show signs of a strongly correlated liquid, as has been advocated recently [39, 40].

To assess these theoretical ideas, computer simulations will certainly be indispensable, since they are presently the only practicable way of obtaining sufficiently detailed information on ionic distributions and correlation functions. The numerical investigations presented in this work and the correlation analysis of the obtained data are a further step in this direction, however a more detailed analysis is presently under way [41].



## 9 Acknowledgments

We wish to thank M. Ballauff, M. Barbosa J. Blaul, B. Guillaume, F. Jimenez-Angeles, K. Kremer, M. Lozada-Cassou and S. May for various contributions to this work. In addition we acknowledge a large computer time grant hkf06 from NIC Jülich and financial support by the German Science foundation.

## Appendix:

### A Defining and computing the pressure

The pressure for the primitive cell model is a nontrivial variable to compute for two reasons: First, the long-range electrostatics has to be properly taken into account, and secondly, the system is inherently anisotropic. Hence, the relevant observable is the stress tensor.

For isotropic systems, the thermodynamic definition of the pressure as the derivative of the free energy with respect to volume leads to the general equation

$$pV = Nk_B T - V \left\langle \frac{\partial U}{\partial V} \right\rangle, \quad (18)$$

where the angular brackets  $\langle \dots \rangle$  denote a canonical average. For the case of short-range interactions the contribution from  $U$  can be further simplified by using

$$\frac{\partial U}{\partial V} = \sum_i \frac{\partial U}{\partial \mathbf{r}_i} \cdot \frac{\partial \mathbf{r}_i}{\partial V} = \sum_i (-\mathbf{F}_i) \cdot \frac{\mathbf{r}_i}{3V}. \quad (19)$$

Substituting this into the pressure equation (18) and using  $\mathbf{F}_{ij} = -\mathbf{F}_{ji}$  gives

$$pV = Nk_B T - \frac{1}{3} \sum_{i < j} \langle \mathbf{r}_{ij} \cdot \mathbf{F}_{ij} \rangle \quad (20)$$

The electrostatic contribution to the pressure can be derived [42] by realizing that the electrostatic energy  $U^C$  is a homogeneous function of volume with degree  $-1/3$ , and hence by Euler's theorem  $\partial U^C / \partial V = -U^C / 3V$ . Adding this to Eqn. (20) finally gives the desired pressure equation

$$pV = Nk_B T - \frac{1}{3} \sum_{i < j} \langle \mathbf{r}_{ij} \cdot \mathbf{F}_{ij}^{\text{sr}} \rangle + \frac{1}{3} \langle U^C \rangle, \quad (21)$$

where  $\mathbf{F}_{ij}^{\text{sr}}$  are the short-range pair forces. Note that for a repulsive hard core the virial contribution is positive, while the electrostatic contribution is one third of the energy density, which for neutral systems is usually negative.

For anisotropic systems the stress tensor is the relevant observable to compute. Whereas the ideal gas contribution to the pressure still remains isotropic, the scalar product in the virial is replaced by the tensor product “ $\otimes$ ”. For the case of electrostatic interactions the derivation is more complicated and will not be presented here. The reader is referred to Ref. [43]. The result is that within the framework of Ewald techniques the electrostatic contribution to the stress

tensor,  $\mathbf{p}^C$ , can be decomposed additively into a real space contribution  $\mathbf{p}^{(r)}$  and a Fourier space contribution  $\mathbf{p}^{(k)}$ . They are given by

$$\mathbf{p}^{(r)}V = \frac{1}{2} \sum_{i,j} q_i q_j \sum_{\mathbf{m} \in \mathbb{Z}^3} \left[ \frac{2\alpha}{\sqrt{\pi}} e^{-\alpha^2 \mathbf{r}_{ij\mathbf{m}}^2} + \frac{\text{erfc}(\alpha |\mathbf{r}_{ij\mathbf{m}}|)}{|\mathbf{r}_{ij\mathbf{m}}|} \right] \frac{\mathbf{r}_{ij\mathbf{m}} \otimes \mathbf{r}_{ij\mathbf{m}}}{|\mathbf{r}_{ij\mathbf{m}}|^2} \quad (22)$$

$$\mathbf{p}^{(k)}V = \frac{1}{2V} \sum_{\mathbf{k} \neq \mathbf{0}} \frac{4\pi}{k^2} e^{-k^2/4\alpha^2} |\tilde{\rho}(\mathbf{k})|^2 \left[ \mathbb{I} - 2 \left( 1 + \frac{k^2}{4\alpha^2} \right) \frac{\mathbf{k} \otimes \mathbf{k}}{k^2} \right]. \quad (23)$$

Here,  $\mathbf{r}_{ij\mathbf{m}} = \mathbf{r}_i - \mathbf{r}_j + \mathbf{m}L_b$ , and the canonical average has not been denoted explicitly. For details of the notation and the Ewald techniques in general, the reader is referred to the literature [21, 22]. Note that the connection to the isotropic case requires the trace of the pressure tensor to be equal to the mean electrostatic energy density, i.e.,  $\text{Tr } \mathbf{p}^C = U^C/V$ .

After computing the electrostatic stress tensor, it can be rotated such that the rod points along the  $z$ -axis. The  $xx$ - and  $yy$ -components of the new tensor then give the pressure perpendicular to the rod, while the  $zz$ -component is the contribution parallel to the rod.

## References

- [1] J.-L. Barrat and J.-F. Joanny, *Advances in Chemical Physics* **94**, 1 (1996).
- [2] *Polyelectrolytes: Science and Technology*, edited by M. Hara (Marcel Dekker, New York, 1993).
- [3] H. Dautzenberg *et al.*, *Polyelectrolytes* (Hanser Verlag, München, 1994).
- [4] S. Förster and M. Schmidt, *Advances in Polymer Science* **120**, 51 (1995).
- [5] W. M. Gelbart, R. F. Bruinsma, P. A. Pincus, and V. A. Parsegian, *Physics Today* **53**, 38 (2000).
- [6] G. L. Gouy, *J. de Phys.* **9**, 457 (1910); D. L. Chapman, *London and Edinburgh Phil. Mag. and J. of Sci.* **25**, 475 (1913).
- [7] T. Alfrey, P. W. Berg, and H. J. Morawetz, *J. Polym. Sci.* **7**, 543 (1951); R. M. Fuoss, A. Katchalsky, and S. Lifson, *Proc. Natl. Acad. Sci. USA* **37**, 579 (1951).
- [8] A. Katchalsky, *Pure Appl. Chem.* **26**, 327 (1971).
- [9] H. Wennerström, B. Jönsson, and P. Linse, *J. Chem. Phys.* **76**, 4665 (1982).
- [10] M. L. Bret and B. Zimm, *Biopolymers* **23**, 271 (1984).
- [11] M. L. Bret and B. Zimm, *Biopolymers* **23**, 287 (1984).
- [12] M. Deserno, C. Holm, and S. May, *Macromolecules* **33**, 199 (2000).
- [13] G. Manning, *J. Chem. Phys.* **51**, 924 (1969).
- [14] F. Oosawa, *Polyelectrolytes* (Marcel Dekker, New York, 1971).

- [15] M. C. Barbosa, M. Deserno, and C. Holm, *Europhys. Lett.* **52**, 80 (2000).
- [16] B. Guilleaume *et al.*, *J. Phys. Cond. Mat.* **12**, A245 (2000).
- [17] J. Blaul, M. Wittemann, M. Ballauff, and M. Rehahn, *J. Phys. Chem. B* **104**, 7077 (2000).
- [18] M. Deserno *et al.*, *Eur. Phys. J. E* **5**, 97 (2001).
- [19] G. S. Grest and K. Kremer, *Phys. Rev. A* **33**, 3628 (1986).
- [20] M. P. Allen and D. J. Tildesley, *Computer Simulation of Liquids*, *Oxford Science Publications*, 1 ed. (Clarendon Press, Oxford, 1987).
- [21] M. Deserno and C. Holm, *J. Chem. Phys.* **109**, 7678 (1998).
- [22] M. Deserno and C. Holm, *J. Chem. Phys.* **109**, 7694 (1998).
- [23] L. Guldbrand, *Mol. Phys.* **67**, 217 (1989).
- [24] L. G. Nilsson, L. Guldbrand, and Nordenskiöld, *Mol. Phys.* **72**, 177 (1991).
- [25] N. Grønbech-Jensen, R. J. Mashl, R. F. Bruinsma, and W. M. Gelbart, *Phys. Rev. Lett.* **78**, 2477 (1997).
- [26] A. P. Lyubartsev, J. X. Tang, P. A. Janmey, and L. Nordenskiöld, *Phys. Rev. Lett.* **81**, 5465 (1998).
- [27] L. Belloni, M. Drifford, and P. Turq, *Chem. Phys.* **83**, 147 (1984).
- [28] E. Allahyarov and H. Löwen, *Phys. Rev. E* **62**, 5542 (2000).
- [29] M. Deserno, Ph.D. thesis, Universität Mainz, 2000.
- [30] M. Deserno, C. Holm, and K. Kremer, in *Physical Chemistry of Polyelectrolytes*, Vol. 99 of *Surfactant science series*, edited by T. Radeva (Marcel Dekker, New York, 2001), Chap. 2, pp. 59–110.
- [31] M. Deserno, *Physica A* **278**, 405 (2000).
- [32] E. Gonzales-Tovar, M. Lozada-Cassou, and D. Henderson, *J. Chem. Phys.* **83**, 361 (1985).
- [33] T. Das, D. Bratko, L. B. Bhuiyan, and C. W. Outhwaite, *J. Phys. Chem.* **99**, 410 (1995).
- [34] T. Das, D. Bratko, L. B. Bhuiyan, and C. W. Outhwaite, *J. Chem. Phys.* **107**, 9197 (1997).
- [35] H. Greberg and R. Kjellander, *J. Chem. Phys.* **108**, 2940 (1998).
- [36] M. Deserno, F. Jiménez-Ángeles, C. Holm, and M. Lozada-Cassou, *Journal Phys. Chem. B*, **105** (44), 10983 (2001).
- [37] J. Neu, *Phys. Rev. Lett.* **82**, 1072 (1999); J. Sader and D. Y. Chan, *J. Colloid Interface Sci.* **213**, 268 (1999).
- [38] E. Trizac and J.-L. Raimbault, *Phys. Rev. E* (2000).

- [39] I. Rouzina and V. Bloomfield, Journal of Phys. Chem. **100**, 9977 (1996).
- [40] B. I. Shklovskii, Phys. Rev. Lett. **82**, 3268 (1999).
- [41] M. Deserno , A. Arnold, and C. Holm, to be published.
- [42] G. Hummer, L. R. Pratt, and A. E. García, J. Phys. Chem. A **102**, 7885 (1998).
- [43] U. Essmann *et al.*, J. Chem. Phys. **103**, 8577 (1995).

## List of Tables:

system	$c$ [g/l]	$T$ [°C]	$\xi$	$\sigma$ [Å]	$d_{\text{ca}}$ [Å]	$R$ [Å]
1	1.5	40	3.4	7.9	4.4	239.3
2	1.5	40	6.8	8.1	4.4	292.0
3	19.95	25	3.32	7.9	4.4	65.6
4	17.99	25	6.64	8.1	4.4	84.3

Table 1: Mapping for four poly(p-phenylene) systems. Tabulated are polyelectrolyte concentration  $c$ , temperature  $T$ , Manning parameter  $\xi$ , ion diameter  $\sigma$ , distance of closest approach  $d_{\text{ca}}$  between ions and the rod and cell radius  $R$  corresponding to the given concentration. The experiments have been performed under salt-free aqueous conditions with monovalent counterions [16].

system	$\hat{p}_{\text{M}}$	$\hat{p}_{\text{PB}}$	$\hat{p}_{\text{MD},1}$	$\hat{p}_{\text{MD},2}$	$\hat{p}_{\text{exp}}$
1	0.1471	0.2128	0.2005(57)	0.201	0.185(15)
2	0.0735	0.1073	0.1003(60)	0.102	0.073(15)
3	0.1506	0.2848	0.2424(57)	0.260	—
4	0.0753	0.1428	0.1215(56)	0.129	—

Table 2: Osmotic coefficient of the four poly(p-phenylene) systems from Table 1. Shown are the Manning limiting law (M), the PB prediction, the simulation result using the stress tensor (MD,1), the simulation result using a PB fit as described in Sec. 4.2 (MD,2) and results from measurements on this system using osmometry [17]

system	$\xi$	$R$ [Å]	$r_0^*$ [Å]	$R_M^*$ [Å]	$\gamma^*$	$\hat{p}^*$
3	3.32	65.6	8.2	28.19	0.957	0.289
4	6.64	84.3	9.9	39.14	1.014	0.153

Table 3: Fit evaluation of small angle X-ray scattering experiments on the systems 3 and 4 [16].  $\xi$  is the Manning parameter,  $R$  the cell radius implied by the polyelectrolyte concentration, and  $r_0^*$  the rod radius, which had been the only fitting parameter. From this, the integration constant  $\gamma^*$  and the Manning radius  $R_M^*$  is determined from the solution of the PB equation.  $\hat{p}^* = (1 + \gamma^{*2})/2\xi$  is the attempt to predict the osmotic coefficient of the solution with the help of the PB formula.

parameter	symbol	value	value in LJ units
ion diameter	$\sigma$	4.25 Å	$\sigma$
ion valence	$v$	2	2
rod radius	$r_0$	7.86 Å	1.85 $\sigma$
line charge density (DNA)	$\lambda$	$e_0/1.7$ Å	2.5 $e_0/\sigma$
Bjerrum length (water)	$\ell_B$	7.14 Å	1.68 $\sigma$
Manning parameter	$\xi$	4.2	4.2
box size	$L_b$	122.4 Å	28.8 $\sigma$
corresponding cell radius	$R$	69.1 Å	16.2 $\sigma$
temperature	$T$	298 K	$\epsilon/k_B$

Table 4: Simulation parameters for a DNA-like system.

## List of Figures

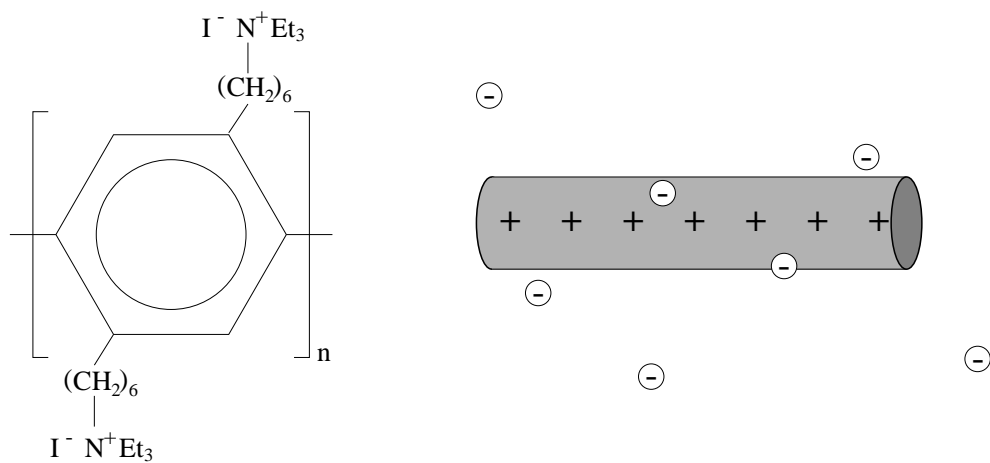


Figure 1: Example of a stiff polyelectrolyte. Constitution formula for poly(para-phenylene) with iodine counterions (left) and a physicist's picture (right).

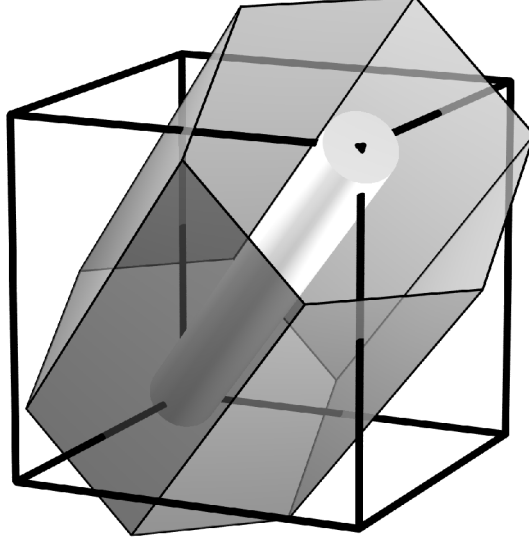


Figure 2: Realization of the cell model. A rod placed along the main diagonal of a cube yields an infinite triangular array of infinitely long rods upon periodic replication of the original cube. The Wigner-Seitz cell of this lattice is a regular hexagon enclosing the rod. This therefore provides a way of obtaining a hexagonal cell without abandoning a cubic geometry.

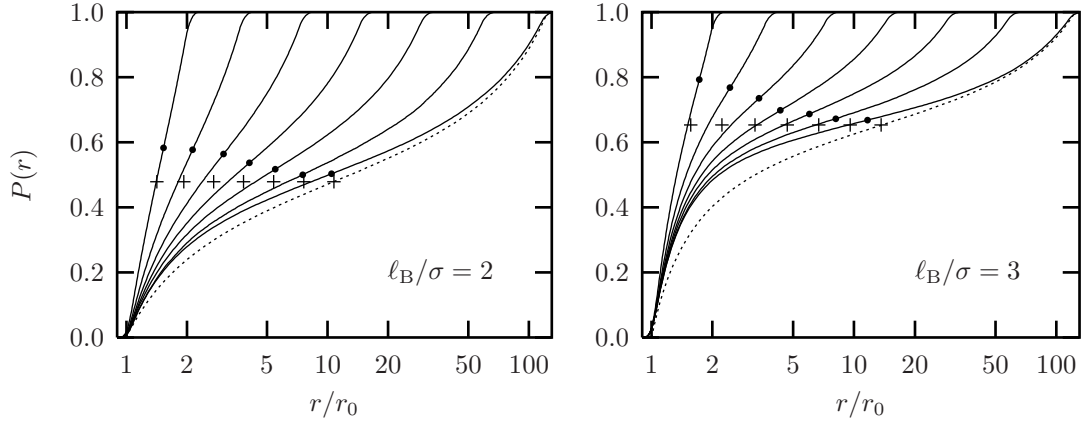


Figure 3: Counterion distribution functions  $P(r)$ , as defined in Eqn. (13), for various simulated densities. Note that an increasing cell radius corresponds to functions extending towards larger values of  $r$ . The heavy dots mark the points of inflection in  $P$  as a function of  $\ln(r)$ , while the crosses mark the positions at which those points would be located on the corresponding PB distribution functions. For the sake of clarity such a PB distribution is only plotted for the system with lowest density, i.e.,  $R = 123.85 \sigma$  (dotted line).



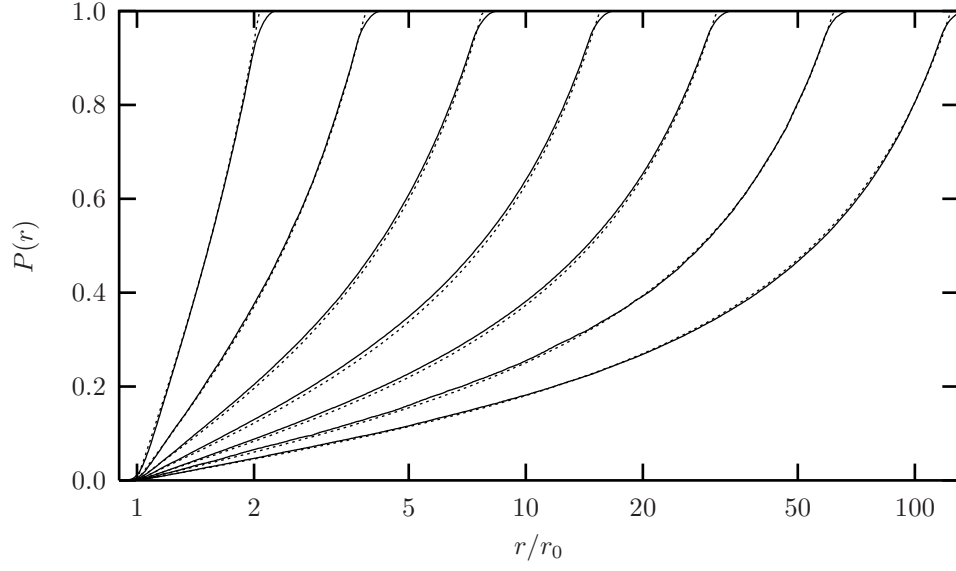


Figure 4: Counterion distribution functions  $P(r)$  (solid lines) for seven systems with the same dimensions as the ones in Fig. 3, but with a Bjerrum length  $\ell_B/\sigma = 1$ . Since the resulting Manning parameter  $\xi = 0.959 < 1$ , counterion condensation is not expected to occur. This is borne out by the observation that the functions are convex up already at  $r = r_0$ . In these weakly charged systems the predictions of PB theory (dotted lines) are excellent and can hardly be distinguished from the simulation results.

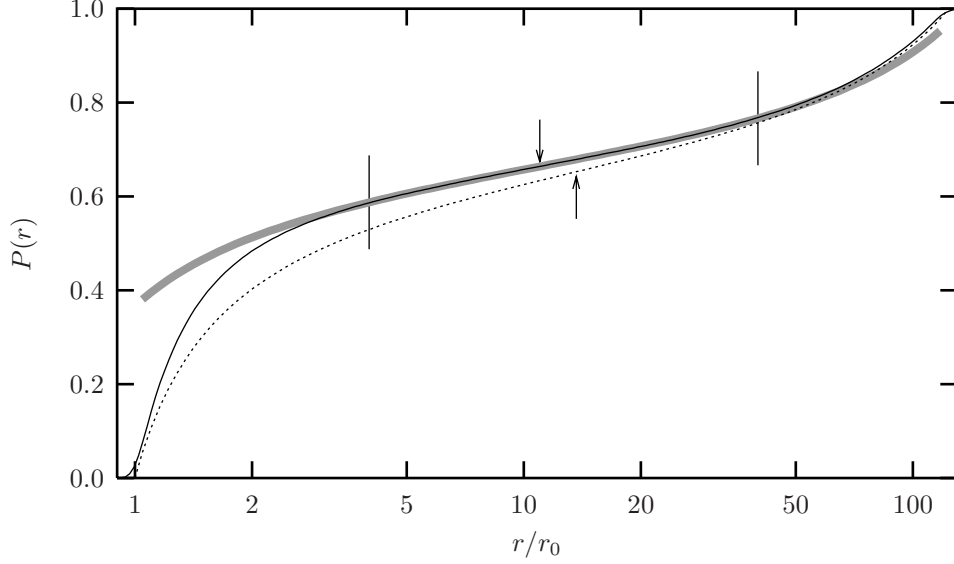


Figure 5: The functional form in Eqn. (14) has been fitted to the measured distribution function (solid line) of the system with  $R = 123.85\sigma$  and  $\ell_B = 3\sigma$  within the range  $[4r_0; 40r_0]$  between the two vertical bars. The  $\uparrow$ -arrow indicates the inflection point of the PB distribution (dotted line), while the  $\downarrow$ -arrow indicates the corresponding point  $(R_M^*; f_M^*) = (11.0\sigma; 0.664)$  of the fit (gray stripe). Note that  $R_M^* < R_M$  although  $f_M^* > f_M$ . The result of the fit is  $\xi^* = 2.97$ ,  $\gamma^* = 0.457$  and  $r_0^* = 0.579\sigma$ .

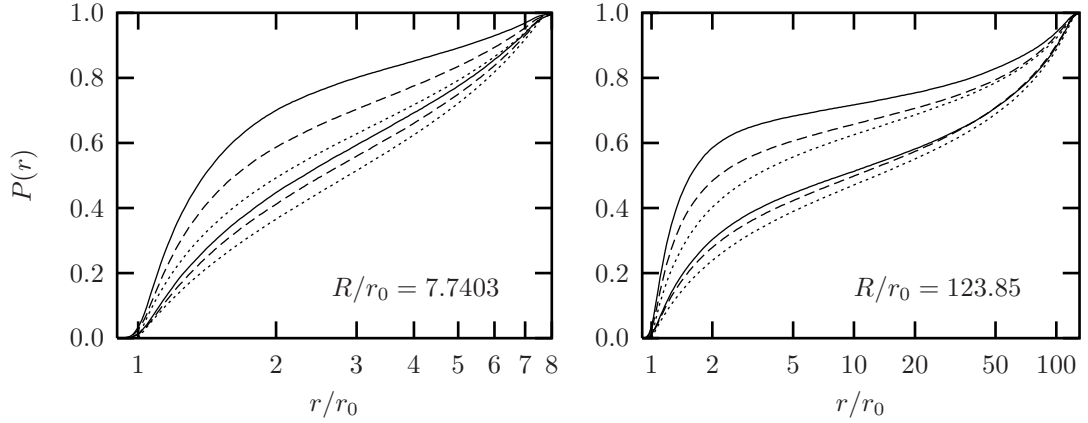


Figure 6: Counterion distribution functions  $P(r)$  versus  $r/r_0$ . The high (low) density situation is shown in the left (right) frame. The lower three curves are for  $v\ell_B/\sigma = 2$ , while the upper three correspond to  $v\ell_B/\sigma = 3$ . The systems with multivalent counterions (solid lines) always show a stronger condensation than the complementary systems with monovalent ions (dashed lines), which themselves show a stronger condensation than PB theory (dotted lines).

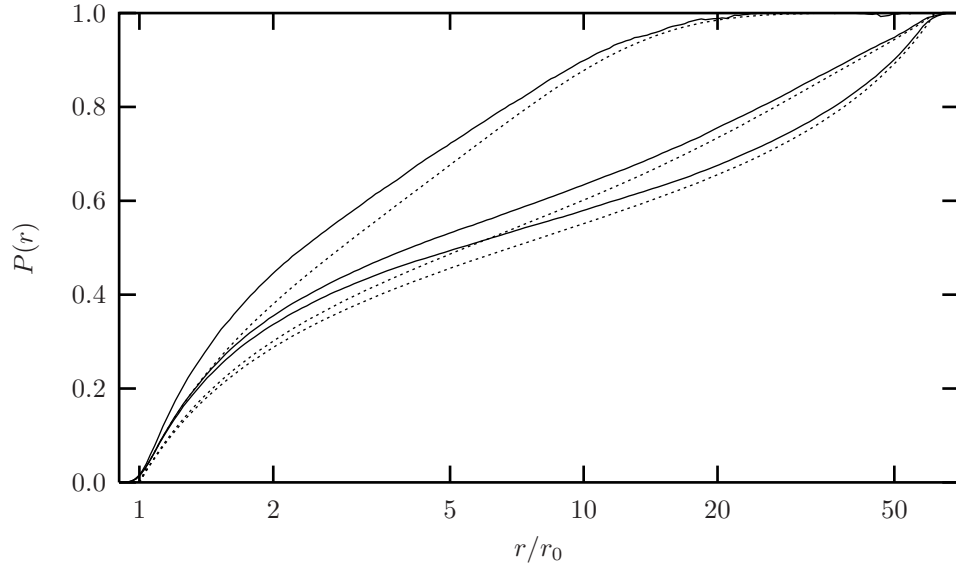


Figure 7: Distribution functions  $P(r)$  for a system which has  $R/\sigma = 61.923$ ,  $\ell_B/\sigma = 2.189$ ,  $\xi = 2.1$  and monovalent ions. From bottom to top the number of salt molecules added to the simulation box of length  $L_b = 144.446\sigma$  is 0, 104 and 3070, which corresponds to a salt Debye length of  $\infty$ ,  $22.9\sigma$  and  $4.2\sigma$ , respectively. The solid lines are the result of a simulation while the dotted lines are the predictions of PB theory.

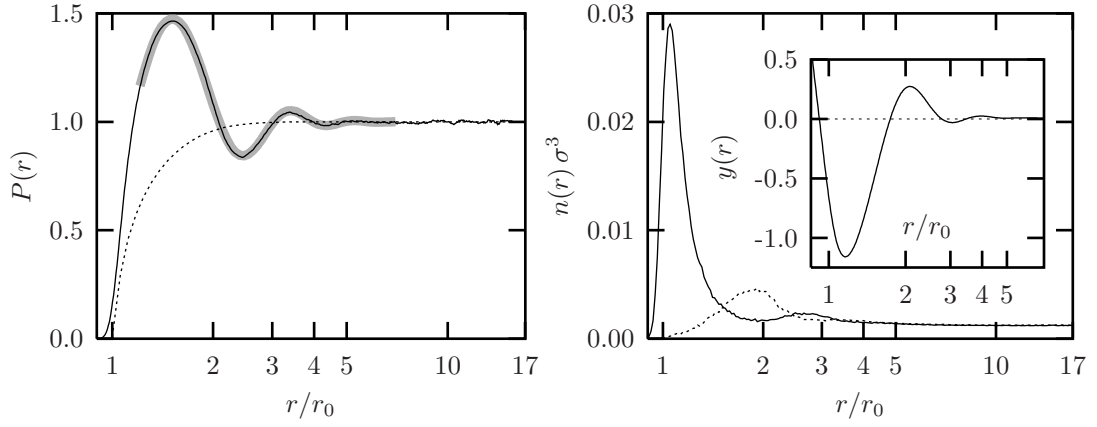


Figure 8: Charge distribution for a system characterized by  $L_b/\sigma = 36.112$ , i.e., 60 monovalent counterions and a cell size of  $R/\sigma = 15.481$ ,  $\ell_B/\sigma = 4.1698$ , i.e.,  $\xi = 4$ , and 1000 molecules of a 2:2 salt within the box volume. The simulation shows a pronounced overcharging-effect in  $P(r)$  (solid curve, left frame), in contrast to PB-theory (dotted curve). The charge oscillations can be described quite accurately by an exponentially damped sine function with period  $1.89\sigma$  and decay length  $0.85\sigma$  (gray stripe). The densities  $n_{-2}(r)$  (solid line, right frame) and  $n_{+2}(r)$  (dotted line) of negative and positive salt ions, respectively, demonstrate the effect of charge layering and local charge reversal, and the inlay shows the dimensionless electrostatic potential  $y(r) = \beta e_0 \psi(r)$ , which is also oscillating.

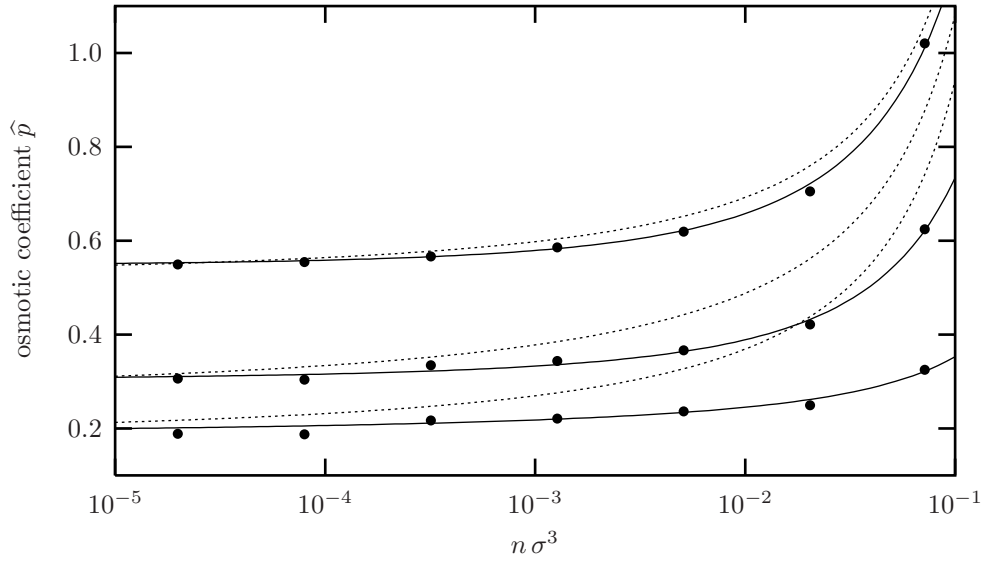


Figure 9: Osmotic coefficient  $\hat{p}$  versus  $n\sigma^3$  for monovalent counterions. Heavy dots mark the measurements, while the solid lines are fits which merely serve to guide the eye. The dotted lines are the prediction of PB theory. From top to bottom the Bjerrum length  $\ell_B/\sigma$  varies as 1,2,3. The errors in the measurement are roughly as big as the dot size.

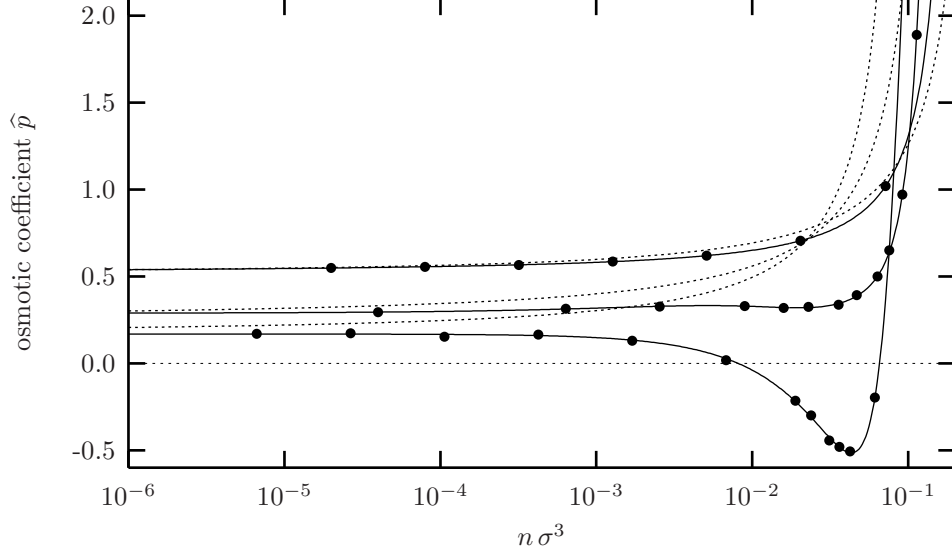


Figure 10: Osmotic coefficient  $\hat{p}$  as a function of density  $n$  for different valences. Heavy dots mark the measurements, while the solid lines are fits which merely serve to guide the eye. The dotted lines are the prediction of PB theory. From top to bottom the counter ion valence  $v$  varies like 1,2,3, which gives the same value of  $\xi v$  as the curves in Fig. 9. The errors in the measurement are roughly as big as the dot size.

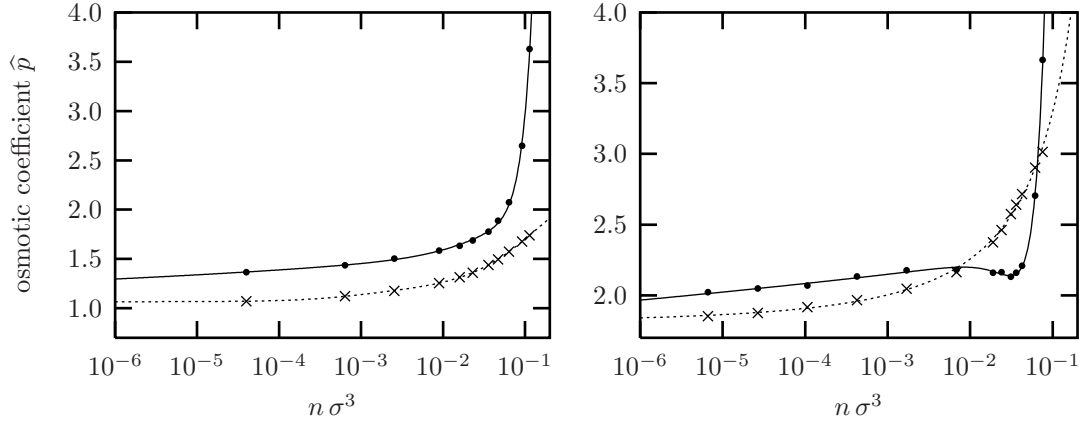


Figure 11: Osmotic coefficient  $\hat{p}$  for the divalent (left) and trivalent (right) systems from Fig. 10, separated into the non-electrostatic contribution coming from virial and ideal gas (heavy dots on solid lines) and negative electrostatic contribution (crosses on dotted lines). Again, the lines are fits which merely serve to guide the eye.

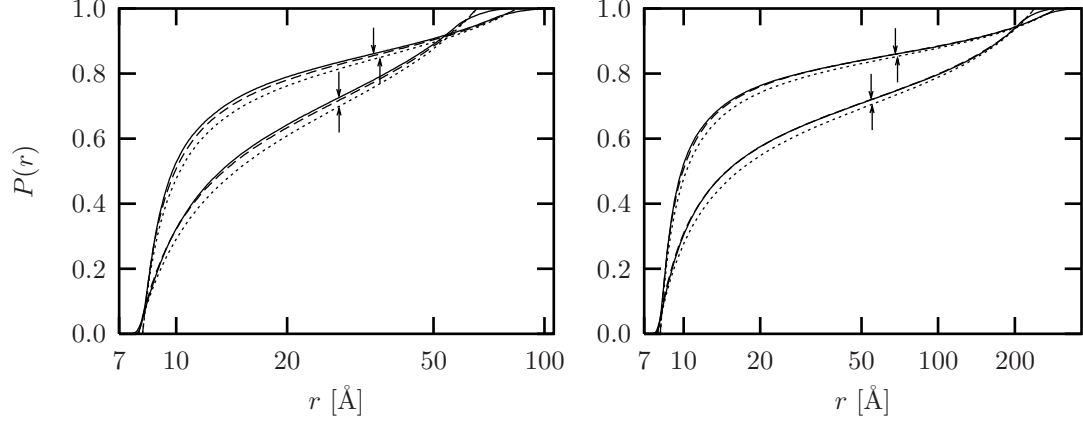


Figure 12: Distribution functions for the 4 poly(p-phenylene) systems from Table 1. Left/right frame correspond to the high/low density systems (3,4)/(1,2), while the upper/lower set of functions correspond to the strongly/weakly charged systems (2,4)/(1,3) respectively. Solid lines are the results of simulation, dotted lines are the PB prediction and dashed lines are from an extended PB theory using the Debye-Hückel-hole-cavity correction [15]. The  $\uparrow$ -arrows indicate the inflection points in the PB distributions, while the  $\downarrow$ -arrows mark those points in the simulated distributions. The deviations of the latter from the PB curves at large  $r$  originate from the simulation cell having a quadratic instead of a circular cross section.

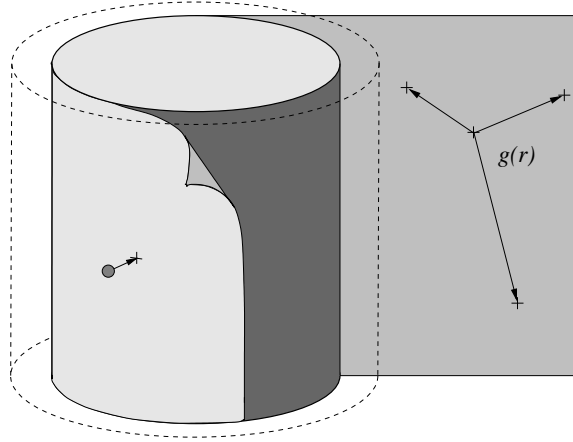


Figure 13: Illustration of the computation of surface correlations. Counterions within a certain small distance from the rod constitute the innermost condensed layer. Their coordinates are radially projected onto the surface, which after that is unrolled to a flat plane. The two-dimensional pair correlation function  $g(r)$  is then determined from the projected points.

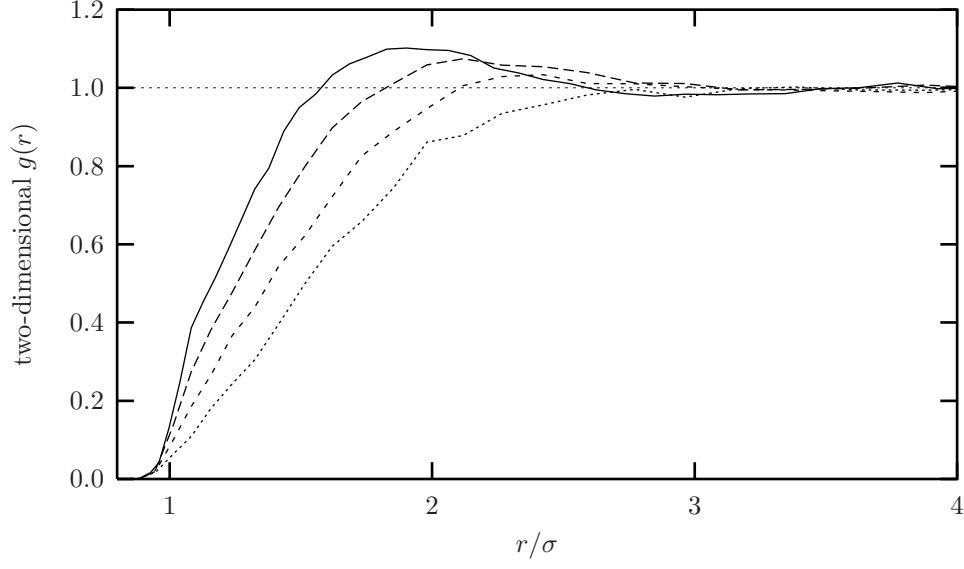


Figure 14: Two-dimensional pair correlation function  $g(r)$  for the projection of counterions within a close condensed layer onto the cylinder of closest approach, see text and Fig. 13. For the four functions the Manning parameter decreases as 10.5, 8.4, 6.3 and 4.2. The last value corresponds to DNA.

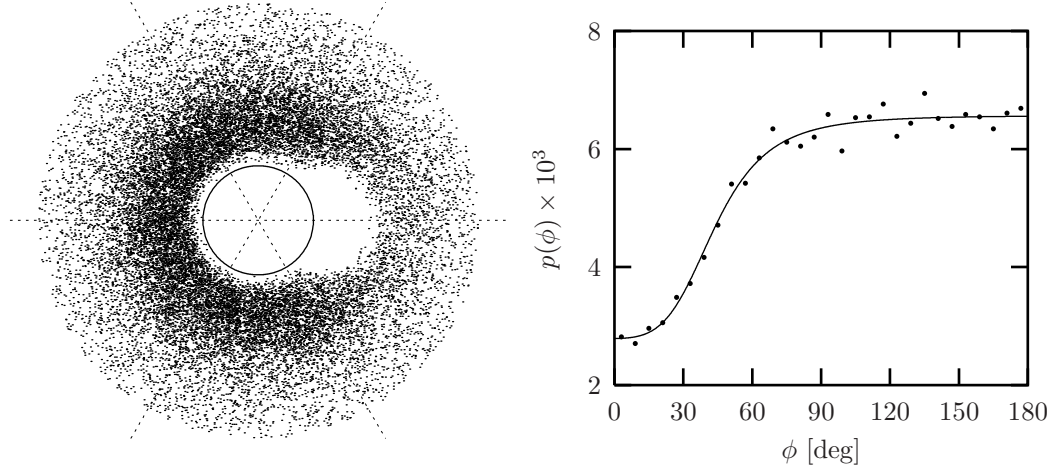


Figure 15: Left part: Density plot of the 3-point correlation function  $g_3(\mathbf{r})$  for the highest charged system from Fig. 14 with Manning parameter  $\xi = 10.5$ . If an ion is located at the origin and its *nearest* neighbor is on the right side and not further away than  $1.3\sigma$ , its *next nearest* neighbor is shown as a dot. The circle around the origin has radius  $\sigma$  and corresponds to the distance of closest approach imposed by the Lennard-Jones potential. The right frame plots the probability distribution of finding the next nearest neighbor at an angle  $\phi$  with respect to a line joining nearest neighbor and origin. The solid line is a guide to the eye.